Three-Antenna Characterization Techniques Employing Spherical Near-Field Scanning With Higher-Order Probe Correction

Gordon Mayhew-Ridgers, *Senior Member, IEEE*, Paul A. van Jaarsveld, *Member, IEEE*, and Johann W. Odendaal, *Senior Member, IEEE*

***Abstract*—The three-antenna technique is typically used in the context of absolute-gain measurements where no gain standard is required. When implemented in a spherical near-field test range, the conventional approach is to use near-field to far-field transformation algorithms with first-order probe correction, which severely limit the choice of antennas that can occupy the probe position. Two new techniques, which are based on higher-order probe correction, are presented. These enable the full characterization of up to three higher-order antennas. The first technique, where only two of the antennas need to occupy the probe position, is useful for the accurate characterization of at least the antenna that is not employed as a probe. The second technique, where all antennas, in turn, occupy the probe position, allows for the accurate characterization of each antenna.**

***Index Terms*—Antenna measurements, antenna radiation patterns, gain measurement, near fields, near-field far-field transformation, probe antennas.**

I. Introduction

ANTENNA gain measurements can be performed with either *gain-transfer* or *absolute-gain* methods [1]. The prior method requires a standard antenna with known gain, while the latter requires no *a priori* knowledge of the antennas. The three-antenna technique is typically used in the context of absolute-gain measurements to characterize three antennas, each with unknown gain, and can be implemented in either far-field or near-field test ranges [2]–[7].

The three-antenna technique involves at least three sets of measurements, taking into account the interaction between all combinations of the three antennas. The result is a system of equations that can be solved to determine the gain of each antenna. When implemented in conjunction with spherical near-field scanning [8], [9], the conventional approach is to mount one of the antennas in the antenna under test (AUT) position while scanning its near field, in turn, with two probe antennas. Most test ranges make use of near-field to far-field transformation algorithms with first-order probe correction [10], [11], thereby limiting the choice for at least the two probe antennas to very elementary antenna types, such as open-ended waveguides. These are mostly narrowband and tend to become very bulky and heavy at lower frequencies. Also, the focus of the conventional three-antenna approach is usually limited to antenna gain only [3], [8], [9].

Two new techniques are introduced here that allow for the full characterization (radiation pattern, gain, and polarization) of up to three higher-order antennas. This enables the simultaneous characterization of more complex and wideband antennas. In addition to the inclusion of higher-order probe-correction algorithms [12]–[14], a new near-field scan sequence was developed, together with the associated post-processing of the measurement data. In terms of the measurement procedure, the first technique is similar to the conventional approach, where two of the antennas are used to occupy the probe position. This is referred to here as the *two-probe three-antenna* (2P3A) technique and is useful for the full characterization of at least the antenna that only occupies the AUT position. In the second technique, all antennas, in turn, occupy the probe position. This is referred to here as the *three-probe three-antenna* (3P3A) technique and allows for the full characterization of all three antennas. The latter technique incorporates the successive over-relaxation method for solving systems of equations [15], [16].

In the sections that follow, both techniques are presented after a brief overview of some aspects related to spherical near-field scanning and the conventional three-antenna technique that are required in the formulation. These new techniques are then numerically and experimentally validated to illustrate their capabilities and applicability.

II. Spherical Near-Field Scanning

The geometry for spherical near-field scanning is shown in Fig. 1, where an AUT in the (x, y, z) coordinate system is scanned by a probe with local coordinate system (x', y', z'). The probe is located at (r, θ, ϕ) in the AUT coordinate system and always points towards its origin (i.e., the z'-axis points in a radial direction defined by θ and ϕ). It can also have a

Manuscript received XX Month XXXX; revised XX Month XXXX; accepted XX Month XXXX. Date of publication XX Month XXXX; date of current version XX Month XXXX. *(Corresponding author: Gordon Mayhew-Ridgers.)*

Gordon Mayhew-Ridgers and Paul A. van Jaarsveld are with Vodacom (Pty) Ltd., Midrand 1635, South Africa (e-mail: gordon.mayhew-ridgers@vodacom.co.za; paul.vanjaarsveld@vodacom.co.za).

Johann W. Odendaal is with the Department of Electrical, Electronic and Computer Engineering, University of Pretoria, Pretoria 0002, South Africa (e-mail: wimpie.odendaal@up.ac.za).

Digital Object Identifier XX.XXXX/TAP.XXXX.XXXXXXX

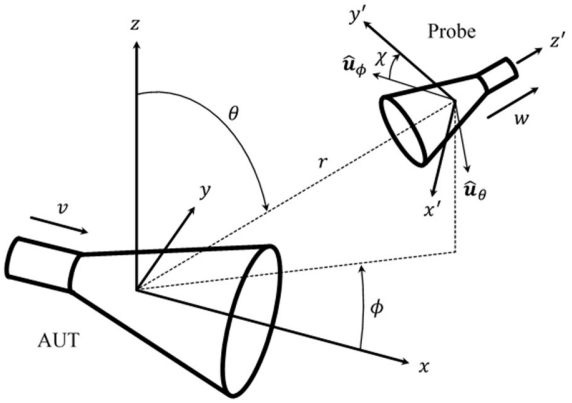

Fig. 1. Geometry for spherical near-field scanning.

rotation angle of χ around the z'-axis (for $\chi = 0$, the x'-axis and $\hat{\boldsymbol{u}}_\theta$ are coincident).

Following mainly the formulation and nomenclature in [10, Sec. 4.3.2] and [12], the near-field transmission equation is expressed as

$$w(r,\chi,\theta,\phi) = v \sum_{smn} T_{smn} \sum_{\mu} P_{s\mu n}(kr) D^n_{\mu m}(\chi,\theta,\phi) \quad (1)$$

where $w(r,\chi,\theta,\phi)$ is the received signal at the probe port and v the excitation at the AUT port (ignoring impedance mismatches for the sake of simplicity). The spherical-wave transmitting coefficients of the AUT are represented by T_{smn}, where the triple summation runs over $s = 1$ and 2, $m = -M \ldots M$, and $n = n_0 \ldots N$. Here, M and N are the truncation numbers for the m and n indices, while $n_0 = \max(|m|, 1)$. The probe response constants for a single-port probe are defined as [10, Sec. 4.3.2]

$$P_{s\mu n}(kr) = \frac{1}{2} \sum_{\sigma\nu} C^{sn}_{\sigma\mu\nu}(kr) R_{\sigma\mu\nu} \quad (2)$$

where k is the wave number and $C^{sn}_{\sigma\mu\nu}(kr)$ are translation coefficients of the spherical vector-wave functions due to the separation of the AUT and probe coordinate systems. The spherical-wave receiving coefficients of the probe are represented by $R_{\sigma\mu\nu}$ (dual-port probes have a unique set of coefficients for each port). The indices associated with the probe run over $\sigma = 1$ and 2, $\mu = -\mu_{\max} \ldots \mu_{\max}$, and $\nu = \nu_0 \ldots \nu_{\max}$ (not to be confused with excitation v). Here, $\mu_{\max}$ and $\nu_{\max}$ are the truncation numbers for the μ and ν indices, while $\nu_0 = \max(|\mu|, 1)$. The receiving and transmitting coefficients of the probe are related through [10, Sec. 5.2.5]

$$R_{\sigma\mu\nu} = (-1)^\mu T_{\sigma,-\mu,\nu}. \quad (3)$$

In (1), $D^n_{\mu n}(\chi,\theta,\phi)$ represents three Euler rotations of the spherical vector-wave functions due to the relative orientations of the AUT and probe coordinate systems. It is defined as [10, Appendix A2]

$$D^n_{\mu n}(\chi,\theta,\phi) = e^{j\mu\chi} d^n_{\mu m}(\theta) e^{jm\phi} \quad (4)$$

where two of the rotations produce phase shifts only, but where $d^n_{\mu m}(\theta)$ represents more complex rotation coefficients.

The far field of the AUT can be evaluated as [10, Sec. 4.3.4]

$$W(\chi,\theta,\phi) = v \sum_{smn} T_{smn} \sum_{\mu} P^{\infty}_{s\mu n} D^n_{\mu m}(\chi,\theta,\phi) \quad (5)$$

which has a very similar form to the near-field transmission equation in (1). Here, $W(\chi,\theta,\phi)$ is the normalized far-field probe signal, while $P^{\infty}_{s\mu n}$ are the normalized far-field probe constants that can be calculated from the receiving coefficients of an electric Hertzian dipole (with χ corresponding to the required far-field polarization).

More concisely, and for further use in this paper, the near-field transmission equation in (1) can now be written in the form of a forward operator

$$w = f_{\mathrm{NF}}\{T_{smn}, R_{\sigma\mu\nu}\} \quad (6)$$

while the far-field transmission equation in (5) can similarly be written as

$$W = f_{\mathrm{FF}}\{T_{smn}\}. \quad (7)$$

The gain of the AUT in the corresponding polarization is given by [10, Sec. 4.3.4]

$$G = (8/3)\,|W|^2/|v|^2\,. \quad (8)$$

The purpose of near-field scanning is to determine the transmitting coefficients of the AUT. This is achieved by inverting the near-field transmission equation and can be concisely written in the form of an inverse operator

$$T_{smn} = f^{-1}_{\mathrm{NF}}\{w, R_{\sigma\mu\nu}\}. \quad (9)$$

Near-field samples are normally required for two orthogonal polarizations. This can typically be obtained with two χ orientations of a calibrated single-port probe or with a single χ orientation of a calibrated dual-port probe. However, in the context of the three-antenna technique, a dual-port probe has to be treated as two separate uncalibrated antennas that require individual characterization. Therefore, two orthogonal probe orientations would still be required.

The operation in (9) can be performed very efficiently for first-order probes where only $|\mu| = 1$ modes are considered and has become the standard approach in most test ranges. Wideband probes, which are becoming more popular, however, require higher-order probe correction. Two such approaches are the FFT/matrix inversion [12] and system-matrix inversion [13] techniques. Both were implemented by the authors, producing similar and accurate results (as was also reported in [14]). While the former was used to produce

the results in this paper, either approach is equally sound.[1]

With the three-antenna technique, some of the antennas are employed both as AUT and as probe. In the AUT coordinate system, the antenna generally points in the $+z$-direction, while in the probe coordinate system, the antenna generally points in the $-z'$-direction. This rotation can be achieved by rotating the probe through 180° around either the x'-axis or the y'-axis, and depends on the convention that is followed in the test range. For a rotation of 180° around the x'-axis, the rotated transmitting coefficients are obtained as

$$T_{\sigma\mu\nu}^{(\mathrm{rot})} = (-1)^{\nu} T_{\sigma,-\mu,\nu} \tag{10}$$

while, for a rotation of 180° around the y'-axis, the relation is

$$T_{\sigma\mu\nu}^{(\mathrm{rot})} = (-1)^{\nu+\mu} T_{\sigma,-\mu,\nu}. \tag{11}$$

III. Conventional Three-Antenna Technique

The scan sequence for the conventional three-antenna technique [3, Sec. 10.6.2.2], [8], [9] is shown in Fig. 2(a), where an AUT, antenna A, is scanned by two probes, first by antenna B and then by antenna C. Finally, the one probe, antenna B, is scanned by the other probe, antenna C.

The receiving coefficients that define the radiation patterns (but not necessarily correct gain) of the two first-order probes, antennas B and C, have to be known in advance to perform probe correction. If not, an additional scan is required where antenna C is scanned by antenna B. As described in [10, Sec. 3.2.5], probe calibration is then implemented via an iterative scheme to first determine the two sets of coefficients. Now, if w_{BC}, for example, represents the near-field samples of antenna B when scanned with two orthogonal orientations of antenna C, the operation in (9) is applied iteratively to determine the two sets of transmitting coefficients as

$$T_{smn}^{\mathrm{B}(l)} = f_{\mathrm{NF}}^{-1}\left\{w_{\mathrm{BC}}, R_{\sigma\mu\nu}^{\mathrm{C}(l-1)}\right\} \tag{12}$$

$$T_{smn}^{\mathrm{C}(l)} = f_{\mathrm{NF}}^{-1}\left\{w_{\mathrm{CB}}, R_{\sigma\mu\nu}^{\mathrm{B}(l)}\right\}. \tag{13}$$

Here, $R_{\sigma\mu\nu}^{\mathrm{B}(l)}$ and $R_{\sigma\mu\nu}^{\mathrm{C}(l)}$ represent the receiving coefficients of antennas B and C during iteration number l, which runs over $l = 1 \ldots L$. Also, the azimuthal mode indices are limited to $|m| = 1$ and $|\mu| = 1$ as required for first-order probe correction. During each iteration, the two antennas are both employed in the roles of AUT (via transmitting coefficients) and probe (via receiving coefficients). The relation in (3), together with that in either (10) or (11), is used to convert between transmitting and receiving coefficients. During the first iteration, $R_{\sigma\mu\nu}^{\mathrm{C}(0)}$ can typically be chosen as the receiving coefficients of an electric Hertzian dipole with appropriate polarization. The process usually converges quite rapidly to the final sets of coefficients, $R_{\sigma\mu\nu}^{\mathrm{B}(L)}$ and $R_{\sigma\mu\nu}^{\mathrm{C}(L)}$, especially if the probes are simple antennas. Note that these coefficients are not necessarily scaled to reflect the actual gains of antennas B and C. The antenna gains associated with the coefficients after L iterations, $G_{\mathrm{B}}^{(L)}$ and $G_{\mathrm{C}}^{(L)}$, will most probably differ from the actual gains, G_{B} and G_{C}. Considering the iterative process in (12) and (13), it can be appreciated that if, for example, the initial receiving coefficients, $R_{\sigma\mu\nu}^{\mathrm{C}(0)}$, produce a gain value that is too low, $G_{\mathrm{C}}^{(L)}$ will also end up being too low, while $G_{\mathrm{B}}^{(L)}$ will be too high.

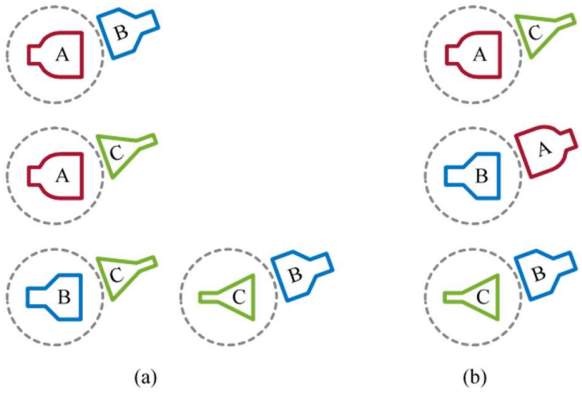

Fig. 2. Scan sequence for three-antenna techniques. (a) Conventional and 2P3A techniques. (b) The 3P3A technique.

By nesting the operations in (7) and (9), near-field to far-field transformations for the three scans on the left in Fig. 2(a) can be written as

$$W_{\mathrm{AB}} = f_{\mathrm{FF}}\left\{f_{\mathrm{NF}}^{-1}\left\{w_{\mathrm{AB}}, R_{\sigma\mu\nu}^{\mathrm{B}(L)}\right\}\right\} \tag{14}$$

$$W_{\mathrm{AC}} = f_{\mathrm{FF}}\left\{f_{\mathrm{NF}}^{-1}\left\{w_{\mathrm{AC}}, R_{\sigma\mu\nu}^{\mathrm{C}(L)}\right\}\right\} \tag{15}$$

$$W_{\mathrm{BC}} = f_{\mathrm{FF}}\left\{f_{\mathrm{NF}}^{-1}\left\{w_{\mathrm{BC}}, R_{\sigma\mu\nu}^{\mathrm{C}(L)}\right\}\right\}. \tag{16}$$

Each of the near-field samples is typically obtained by making use of a bypass measurement where the cables to the AUT and probe ports are either connected directly or through a separate cable (and possibly attenuator) with known losses. As such, cable losses in the system are calibrated out and it can be assumed that $v = 1$.

It can furthermore be shown that, by using the expression in (8) and by realizing that $R_{\sigma\mu\nu}^{\mathrm{B}(L)}$ and $R_{\sigma\mu\nu}^{\mathrm{C}(L)}$ are effectively scaled by $\left(G_{\mathrm{B}}^{(L)}/G_{\mathrm{B}}\right)^{1/2}$ and $\left(G_{\mathrm{C}}^{(L)}/G_{\mathrm{C}}\right)^{1/2}$, it is possible to express (14) to (16) as products of the actual antenna gains:

$$G_{\mathrm{A}}G_{\mathrm{B}} = (8/3)|W_{\mathrm{AB}}|^2 G_{\mathrm{B}}^{(L)} = M_{\mathrm{AB}} \tag{17}$$

$$G_{\mathrm{A}}G_{\mathrm{C}} = (8/3)|W_{\mathrm{AC}}|^2 G_{\mathrm{C}}^{(L)} = M_{\mathrm{AC}} \tag{18}$$

$$G_{\mathrm{B}}G_{\mathrm{C}} = (8/3)|W_{\mathrm{BC}}|^2 G_{\mathrm{C}}^{(L)} = M_{\mathrm{BC}}. \tag{19}$$

These three equations are then solved to determine the actual gain of each of the three antennas as

[1] When using the system-matrix inversion approach in [13] to implement the three-antenna characterization techniques in this paper, the probe should be modeled with a spherical-wave expansion as opposed to complex dipoles.

$$G_{\mathrm{A}} = (M_{\mathrm{AB}} M_{\mathrm{AC}} / M_{\mathrm{BC}})^{1/2} \tag{20}$$

$$G_{\mathrm{B}} = (M_{\mathrm{AB}} M_{\mathrm{BC}} / M_{\mathrm{AC}})^{1/2} \tag{21}$$

$$G_{\mathrm{C}} = (M_{\mathrm{AC}} M_{\mathrm{BC}} / M_{\mathrm{AB}})^{1/2}. \tag{22}$$

IV. Higher-Order Two-Probe Three-Antenna Technique

Higher-order probe correction allows for more complex and wideband antennas to be used as near-field probes, which of course brings about many benefits. The conventional three-antenna technique can be extended to fully characterize an AUT with two higher-order probes while still following the scan sequence (all four scans) in Fig. 2(a).

It is assumed that the receiving coefficients of the probes are not known in advance. However, by using the iterative scheme as described in the previous section, together with higher-order probe correction, it is possible to determine these coefficients. Depending on the choice of the initial coefficients, $R_{\sigma\mu\nu}^{\mathrm{C}(0)}$, in (12), the final coefficients for the two probes can either converge to the correct form (usually the case for antennas with predominantly linear polarization) or not. However, in either case, it is still possible to obtain the correct results for at least the AUT, which is not employed as a probe.

As with the conventional three-antenna technique, near-field to far-field transformations for the three scans on the left in Fig. 2(a) are also represented by the expressions in (14) to (16). In this case, however, the higher-order receiving coefficients that emanate from the iterative process in (12) and (13) are used. The products of the actual antenna gains for the scans follow from the expressions in (17) to (19), while the actual gain of each of the three antennas can once again be determined with the expressions in (20) to (22).

The transformations in (14) and (15) both produce far fields for antenna A: W_{AB} with antenna B as the probe and W_{AC} with antenna C as the probe. Now, as has been explained in the previous section, it is possible, for example, that after running the iterative process in (12) and (13), the $R_{\sigma\mu\nu}^{\mathrm{B}(L)}$ coefficients are too high with the $R_{\sigma\mu\nu}^{\mathrm{C}(L)}$ coefficients being too low. As such, W_{AB} will be too low, while W_{AC} will be too high. It then follows intuitively that W_{AB} and W_{AC} could be averaged to determine the correct far field. Numerical experimentation has revealed that this is indeed the case, but that the solution is actually more stable (especially when the $R_{\sigma\mu\nu}^{\mathrm{C}(0)}$ coefficients in (12) do not represent such a good initial guess) if the far fields are first converted to left-handed, $W_{\mathrm{AB}}^{\mathrm{L}}$ and $W_{\mathrm{AC}}^{\mathrm{L}}$, as well as right-handed, $W_{\mathrm{AB}}^{\mathrm{R}}$ and $W_{\mathrm{AC}}^{\mathrm{R}}$, circularly polarized components before calculating the average fields as

$$W_{\mathrm{A}}^{\mathrm{L}} = \left(\left|W_{\mathrm{AB}}^{\mathrm{L}}\right|\left|W_{\mathrm{AC}}^{\mathrm{L}}\right|\right)^{1/2} e^{j[\arg(W_{\mathrm{AB}}^{\mathrm{L}})+\arg(W_{\mathrm{AC}}^{\mathrm{L}})]/2} \tag{23}$$

$$W_{\mathrm{A}}^{\mathrm{R}} = \left(\left|W_{\mathrm{AB}}^{\mathrm{R}}\right|\left|W_{\mathrm{AB}}^{\mathrm{R}}\right|\right)^{1/2} e^{j[\arg(W_{\mathrm{AB}}^{\mathrm{R}})+\arg(W_{\mathrm{AC}}^{\mathrm{R}})]/2}. \tag{24}$$

In these expressions, the phase should be unwrapped and equalized in the main beam of the AUT before performing the calculations. The resulting far fields, $W_{\mathrm{A}}^{\mathrm{L}}$ and $W_{\mathrm{A}}^{\mathrm{R}}$, can be converted back to the desired polarization basis and should produce the correct radiation pattern and gain for antenna A, regardless of the accuracy of these values for antennas B and C. If the $R_{\sigma\mu\nu}^{\mathrm{C}(0)}$ coefficients in (12) represent a good initial guess, it has been observed that either the linearly polarized far-field components, or the transmitting coefficients themselves, can also be averaged.

V. Higher-Order Three-Probe Three-Antenna Technique

With higher-order probe correction, any three antennas can in principle be employed both in the roles of AUT and probe, provided that it is physically possible. An alternative scan sequence, as shown in Fig. 2(b), then becomes feasible. In this case, antenna A is first scanned by antenna C. Antenna A then becomes the probe for scanning antenna B, after which antenna B finally becomes the probe for scanning antenna C. In this way, each antenna is scanned by one antenna, while it is also used, in turn, to scan another antenna.

Expanding upon the probe calibration process in (12) and (13), the operation in (9) can be applied iteratively to determine three sets of coefficients. However, by following an approach that is very similar to the successive over-relaxation method, which can be used to solve systems of equations with increased convergence rate [15], [16, Sec. 3.3], the iterative process is adapted so that each iteration also contains a contribution from the previous iteration:

$$T_{smn}^{\mathrm{A}(l)} = \alpha f_{\mathrm{NF}}^{-1}\left\{w_{\mathrm{AC}}, R_{\sigma\mu\nu}^{\mathrm{C}(l-1)}\right\} + (1-\alpha) T_{smn}^{\mathrm{A}(l-1)} \tag{25}$$

$$T_{smn}^{\mathrm{B}(l)} = \alpha f_{\mathrm{NF}}^{-1}\left\{w_{\mathrm{BA}}, R_{\sigma\mu\nu}^{\mathrm{A}(l)}\right\} + (1-\alpha) T_{smn}^{\mathrm{B}(l-1)} \tag{26}$$

$$T_{smn}^{\mathrm{C}(l)} = \alpha f_{\mathrm{NF}}^{-1}\left\{w_{CB}, R_{\sigma\mu\nu}^{\mathrm{B}(l)}\right\} + (1-\alpha) T_{smn}^{\mathrm{C}(l-1)}. \tag{27}$$

Here, α is used to control the relative contributions from the current and previous iterations. A value of $\alpha < 1$ must be used for the coefficients in (25) to (27) to converge to their final values. It was found through numerical experimentation that a value of $\alpha = 0.8$ produces satisfactory results.

During the first iteration, $R_{\sigma\mu\nu}^{\mathrm{C}(0)}$ can once again be chosen as the receiving coefficients of an electric Hertzian dipole. The 3P3A technique appears to be much more robust than the 2P3A technique in terms of the choice of the initial coefficients. Regardless of whether the initial choice is a good approximation or not, it has been found through numerical experimentation that the final coefficients converge to the correct values. The far-field radiation patterns and gains of all three antennas can of course be calculated again with the expressions in (7) and (8). As the iterative process for the 2P3A technique only contains two sets of equations that are not completely independent, the successive over-relaxation method does not improve the results.

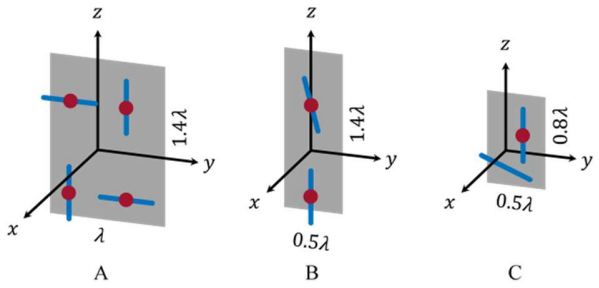

Fig. 3. Antennas for numerical validation.

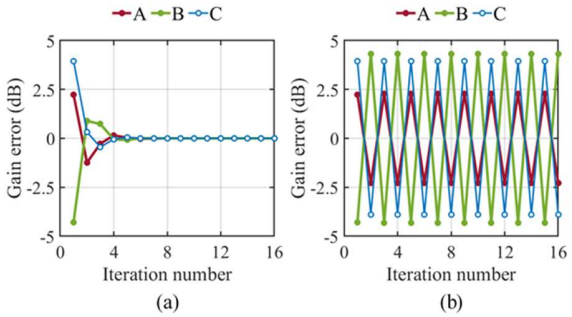

Fig. 4. Convergence of the gain error as a function of the iteration number l for antennas A, B, and C in the simulated 3P3A technique. (a) $\alpha = 0.8$. (b) $\alpha = 1$.

VI. Numerical Validation

In order to validate and compare the new three-antenna characterization techniques under equally challenging conditions, three different antennas, as shown in Fig. 3, were simulated with the Feko method-of-moments solver [17]. These three antennas each comprise dipole elements of length 0.46λ that are arranged at a distance of 0.25λ in front of a rectangular reflector. The models for antennas A and B also include feed networks (not shown) to provide single ports. Antenna A features four driven dipole elements that are configured to produce right-handed circular polarization together with squint of its main beam. Antenna B features two driven dipole elements that produce predominantly linear polarization with some cross polarization and squint of the main beam. Antenna C features one driven dipole element and one slanted parasitic dipole element, arranged to produce predominantly linear polarization with relatively high levels of cross polarization.

The far-field radiation pattern of each antenna was calculated with Feko, after which the expression in (7) was inverted to determine the transmitting coefficients. The near-field transmission equation in (1) can be evaluated very rapidly over the surface of a sphere [13] and was used to simulate the various near-field scans that were required. Although this approach does not include multiple reflections between the AUT and probe, it provided near-identical results to similar but much lengthier simulations with Feko. The radiated power associated with higher-order modes is approximately 48% for antenna A, 70% for antenna B, and 53% for antenna C. Maximum mode numbers of $N = M = 9$ were used for each antenna.

The scan sequences for the two techniques corresponded to the outlines in Fig. 2. For the 2P3A technique, antenna A only occupied the AUT position, while antennas B and C occupied both AUT and probe positions. For the 3P3A technique, antenna A was scanned by antenna C, antenna B by antenna A, and antenna C by antenna B. In both cases, the iterations were initiated by setting the initial receiving coefficients of antenna C equal to those of an electric Hertzian dipole. In all cases, the scan radius was 6λ and the angular increments 15° along both the θ and ϕ directions.

The iterative process in (12) and (13) for the 2P3A technique, as well as that in (25) to (27) for the 3P3A technique, converges rapidly. It is shown in Fig. 4 how the gain error converges toward zero (less than 0.001 dB after 9 iterations) for all three antennas when using the 3P3A technique with $\alpha = 0.8$, but that the gain error oscillates between low and high values when $\alpha = 1$. In the latter case, the initial gain of antenna C is too low due to the Hertzian-dipole approximation. As this antenna is then used to scan antenna A, the calculated gain of antenna A becomes too high. In a similar way, the calculated gain of antenna B becomes too low, while that of antenna C becomes too high. On the next iteration, the errors are inverted. When $\alpha = 1$, it turns out, that after a few iterations, the average value of two consecutive iterations is quite close to the correct gain for each antenna. The 2P3A technique achieves a gain error of less than 0.001 dB for antenna A, but more than 2 dB for antenna B and more than 1.7 dB for antenna C.

The final far-field radiation patterns, as obtained via both the 2P3A and 3P3A ($\alpha = 0.8$) techniques, for each of the three antennas, are compared to reference patterns in Figs. 5 to 7. The difference between the patterns can be expressed as an equivalent noise level in the corresponding plane [18]. In the case of the 3P3A technique, the difference between the final and reference patterns is less than -80 dB in both planes for all three antennas. Numerical experimentation has also shown that similar results can be obtained via different scan sequences and by initiating the iterative process with any of the antennas, even antenna A that has circular polarization. In the case of the 2P3A technique, the results for antenna A, which only occupied the AUT position, also have a difference between the final and reference patterns of less than -80 dB in both planes. The results for the other two antennas show much larger differences when compared to the references, both in terms of realized gain and shape of the radiation patterns, especially for the predominantly cross-polar ones. Numerical experimentation has shown that accurate results for antennas B and C can be obtained if the initial Hertzian-dipole approximation is improved. This can, for example, be achieved by using an antenna with low cross polarization to initiate the iterative process.

VII. Experimental Validation

The four antennas in Fig. 8 were used to validate the new three-antenna characterization techniques with actual measurements. These were performed in the compact antenna

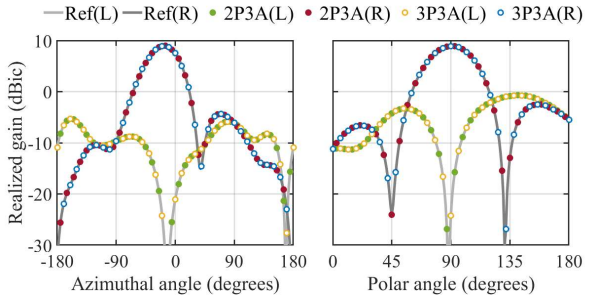

Fig. 5. Simulated far-field radiation patterns for antenna A as a function of the azimuthal angle ϕ ($\theta = 90°$) and polar angle θ ($\phi = -20°$). The traces correspond to left-handed (L) and right-handed (R) circular polarizations.

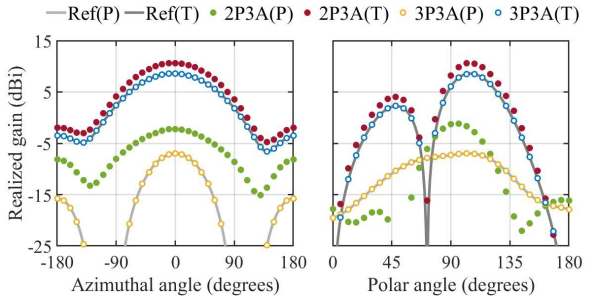

Fig. 6. Simulated far-field radiation patterns for antenna B as a function of the azimuthal angle ϕ ($\theta = 105°$) and polar angle θ ($\phi = 0°$). The traces correspond to $\hat{\boldsymbol{u}}_\phi$-directed (P) and $\hat{\boldsymbol{u}}_\theta$-directed (T) linear polarizations.

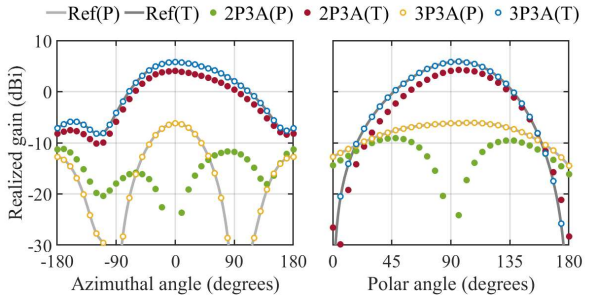

Fig. 7. Simulated far-field radiation patterns for antenna C as a function of the azimuthal angle ϕ ($\theta = 90°$) and polar angle θ ($\phi = 0°$). The traces correspond to $\hat{\boldsymbol{u}}_\phi$-directed (P) and $\hat{\boldsymbol{u}}_\theta$-directed (T) linear polarizations.

test range at the University of Pretoria, which has been upgraded by the authors during recent years to also accommodate near-field antenna measurements [19]. The two quad-ridged horns and the double-ridged horn were used for validating the 3P3A technique, while the two quad-ridged horns and the base-station reference antenna were used for validating the 2P3A technique.

Measurements for the 3P3A technique spanned the 650–4000 MHz frequency band, while those for the 2P3A technique were confined to the 1400–2700 MHz frequency band. In both cases, a sampling interval of 5 MHz was used, together with time gating to reduce the effect of reflections within the chamber. Maximum mode numbers of $N = M = 42$ were considered for each antenna in the 3P3A technique, while $N = M = 35$ for the horns and $N = M = 40$ for the base-station reference antenna were considered for the 2P3A technique. The radiated power associated with higher-order

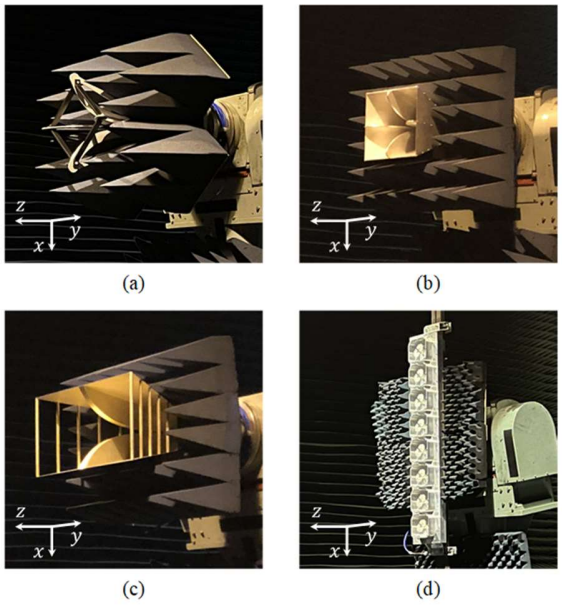

Fig. 8. Antennas for experimental validation. (a) Open-boundary quad-ridged horn. (b) Closed-boundary quad-ridged horn. (c) Double-ridged horn. (d) Base-station reference antenna.

modes at 2350 MHz is approximately 24% for the open-boundary quad-ridged horn, 18% for the closed-boundary quad-ridged horn, 12% for the double-ridged horn, and 61% for the base-station reference antenna. The open-boundary quad-ridged horn was embedded in microwave absorbing material, while the other antennas were shielded from the AUT and probe positioners with absorbing collars. Uncertainties due to impedance mismatches were reduced by inserting 10 dB attenuators at both the AUT and probe ports.

For the 3P3A technique, the open-boundary quad-ridged horn was scanned by the double-ridged horn, the closed-boundary quad-ridged horn by the open-boundary quad-ridged horn, and the double-ridged horn by the closed-boundary quad-ridged horn. Scan radii of 2319 mm and 2343 mm were used, while the angular increments were 3.75° along both the θ and ϕ directions. The receiving coefficients of the double-ridged horn were initially set equal to those of an electric Hertzian dipole, while a value of $\alpha = 0.8$ was used in the iterative solution. For the 2P3A technique, the base-station reference antenna only occupied the AUT position, while the two quad-ridged horns were used as probes. A scan radius of 2581 mm was used, while the angular increments were 5° along both the θ and ϕ directions. The receiving coefficients of the closed-boundary quad-ridged horn were initially approximated by those of an electric Hertzian dipole and were also used to initiate the iterative process for determining the coefficients of the two quad-ridged horns.

The results for the open-boundary quad-ridged horn are shown in Figs. 9 and 10. The normalized co-polar and cross-polar far-field radiation patterns (according to Ludwig's third definition [20]) on a plane diagonally through the aperture of the horn are compared for the 3P3A and 2P3A techniques at a single frequency in Fig. 9, while the realized gain as a function of frequency is compared in Fig. 10. The difference between

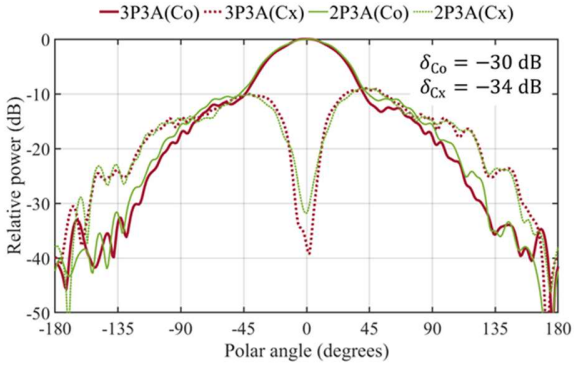

Fig. 9. Normalized co-polar (Co) and cross-polar (Cx) far-field radiation patterns at 2350 MHz for the open-boundary quad-ridged horn as a function of the polar angle θ in a diagonal plane ($\phi = -45°$).

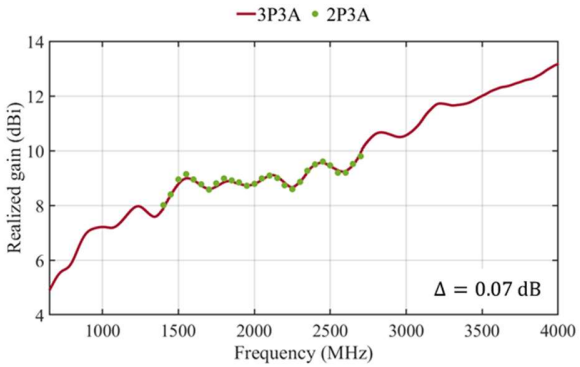

Fig. 10. Realized gain of the open-boundary quad-ridged horn.

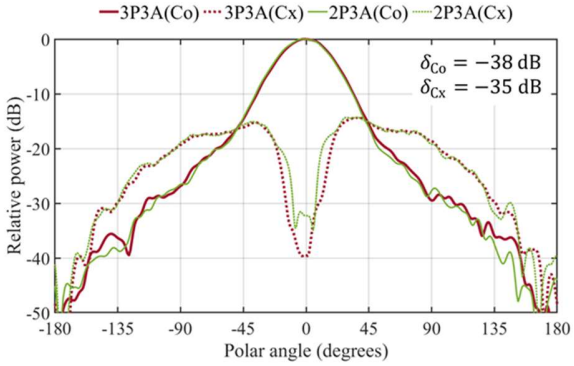

Fig. 11. Normalized co-polar (Co) and cross-polar (Cx) far-field radiation patterns at 2350 MHz for the closed-boundary quad-ridged horn as a function of the polar angle θ in a diagonal plane ($\phi = -45°$).

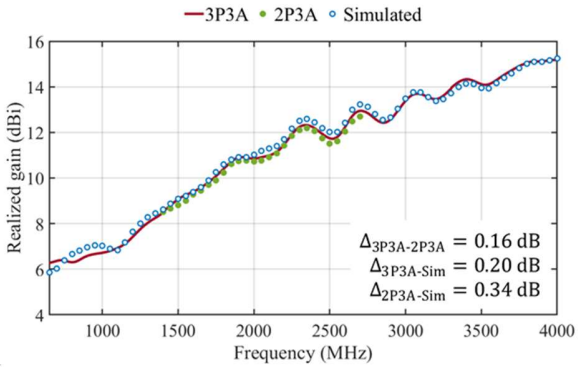

Fig. 12. Realized gain of the closed-boundary quad-ridged horn.

these patterns is expressed as equivalent noise levels [18] in the forward hemisphere of the corresponding plane: δ_{Co} for the co-polar pattern and δ_{Cx} for the cross-polar pattern. The gain difference, Δ, is expressed as the root-mean-square value over frequency.

Similar results for the closed-boundary quad-ridged horn are shown in Figs. 11 and 12. In this case, a detailed numerical model of the horn was available. As the horn only consists of metallic parts, and assuming losses are negligible, its realized gain was calculated by subtracting the measured impedance-mismatch factor from the simulated directivity [21]. The simulation model did not include any microwave absorbing material and it can also be seen at the low end of the frequency band that interaction between the antenna and the AUT positioner probably affected the measurements somewhat.

Validation results for the double-ridged horn are shown in Figs. 13 and 14. Once again, normalized co-polar and cross-polar far-field radiation patterns on a diagonal plane through the aperture of the horn are compared in Fig. 13. In this case, results from the 3P3A technique are compared to results that were measured directly in the far field using the compact antenna test range (CATR) at the University of Pretoria. Reference gain values were also obtained from a national calibration laboratory. These are compared to the values from the 3P3A technique in Fig. 14. Once again, it has to be noted that the reference values do not include effects due to microwave absorbing material.

Finally, measured results for the base-station reference antenna are shown in Figs. 15 to 17. For this antenna, a detailed numerical model, as well as a duplicate feed network, was available to produce simulated reference data. As the antenna consists mostly of metallic parts, the realized gain was calculated by subtracting the measured impedance-mismatch factor and losses in the feed network from the simulated directivity. Also, separate gain measurements were perfomermed via the gain-transfer method on a cylindrical near-field system. In this case, a Scientific-Atlanta standard-gain horn was used as the gain reference. Its gain was calculated by subtracting the measured impedance-mismatch factor from its simulated directivity. The latter can be calculated very accuratley via numerical methods [21], [22]. Normalized co-polar and cross-polar far-field radiation patterns from the 3P3A technique are compared to simulated patterns in Fig. 15 for the azimuth plane of the antenna and in Fig. 16 for the elevation plane of the antenna. Towards the rear of the antenna, the microwave absorbing material and AUT positioner affected the radiation patterns. The realized-gain values from the 3P3A technique are compared to those from the cylindrical near-field gain-transfer measurements (CNF GTM) and simulations in Fig. 17.

VIII. Conclusion

Two new techniques have been introduced to enable three-antenna characterization measurements in a spherical near-

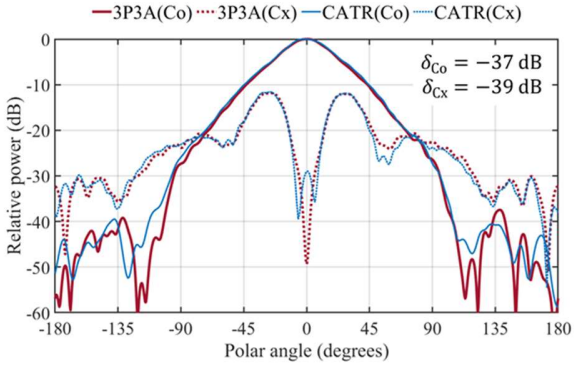

Fig. 13. Normalized co-polar (Co) and cross-polar (Cx) far-field radiation patterns at 2350 MHz for the double-ridged horn as a function of the polar angle θ in a diagonal plane ($\phi = -45°$).

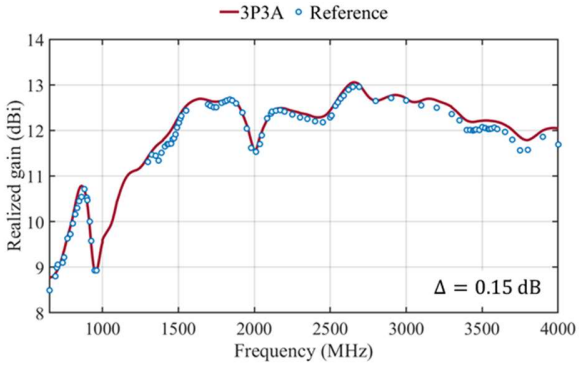

Fig. 14. Realized gain of the double-ridged horn.

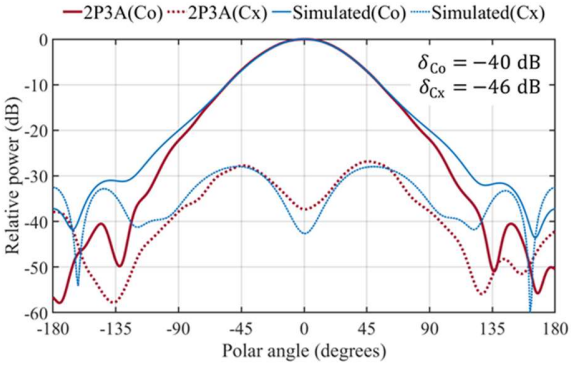

Fig. 15. Normalized co-polar (Co) and cross-polar (Cx) far-field radiation patterns at 2350 MHz for the base-station reference antenna as a function of the polar angle θ in the azimuthal plane ($\phi = 90°$).

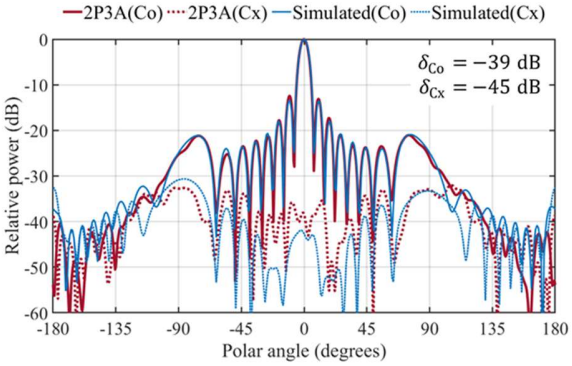

Fig. 16. Normalized co-polar (Co) and cross-polar (Cx) far-field radiation patterns at 2350 MHz for the base-station reference antenna as a function of the polar angle θ in the elevation plane ($\phi = 0°$).

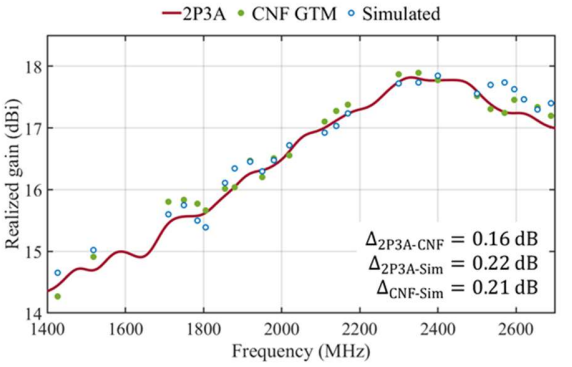

Fig. 17. Realized gain of the base-station reference antenna.

field antenna test range using higher-order probe antennas. As opposed to the conventional three-antenna technique, which only allows for first-order antennas to be employed as probes, it has been confirmed through numerical simulations and actual measurements that the two new three-antenna techniques can characterize up to three higher-order antennas in terms of gain and full radiation-pattern information over a wide band of frequencies. This is very beneficial when special first-order probes are not available or when multiple near-field scans would otherwise have been required when using these usually narrowband probes. Both new techniques are based on higher-order probe-correction algorithms, but differ in terms of the scan sequence of the antennas and the post-processing of the measurements.

The 2P3A technique allows for the characterization of three antennas where it is impossible to deploy one of the antennas in the probe position. This technique requires four sets of near-field scans if the receiving coefficients of the two antennas, which are deployed in the probe position, are not known in advance. It provides accurate results for the antenna that is only deployed in the AUT position, but the accuracy for the other two antennas depends on how well the initial guess approximates the receiving coefficients of the antenna that is used to initiate the iterative solution process.

The 3P3A technique provides accurate results for all three antennas, but requires that all antennas, in turn, be deployed in both the AUT and probe positions. It involves three sets of near-field scans, following any sequence and using any of the antennas to initiate the iterative solution. The method is very robust in terms of the initial receiving coefficients that is chosen for the first antenna as long as a value of $\alpha < 1$ is used in the iterative process.

REFERENCES

[1] C. A. Balanis, *Antenna Theory: Analysis and Design*, 2nd ed. New York: John Wiley & Sons, 1997.

[2] *IEEE Standard Test Procedures for Antennas*, IEEE Standard 149-1979, 1979.

[3] C. Parini, S. Gregson, J. McCormick, and D. J. Janse van Rensburg, *Theory and Practice of Modern Antenna Range Measurements*. London, U.K.: The Institution of Engineering and Technology, 2014.

[4] H. Shakhtour, R. Cornelius, and D. Heberling, "Three antenna gain determination method in compact antenna test ranges," in *Proceedings of the Loughborough Antennas and Propagation Conference (LAPC)*, Loughborough, U.K., Nov. 11–12, 2013, pp. 392–396.

[5] A. C. Newell, C. F. Stubenrauch, and R. C. Baird, "Calibration of microwave antenna gain standards," *Proc. IEEE*, vol. 74, no. 1, pp. 129–132, Jan. 1986.

[6] A. C. Newell, R. C. Baird, and P. F. Wacker, "Accurate measurement of antenna gain and polarization at reduced distances by an extrapolation technique," *IEEE Trans. Antennas Propag.*, vol. AP-21, no. 4, pp. 418–431, Jul. 1973.

[7] A. C. Newell, R. D. Ward, and E. J. McFarlane, "Gain and power parameter measurements using planar near-field techniques," *IEEE Trans. Antennas Propag.*, vol. 36, no. 6, pp. 792–803, Jun. 1988.

[8] G. Masters and P. Pelland, "Selection criteria for near-field gain techniques," in *Proc. Antenna Meas. Techn. Assoc. Symp. (AMTA)*, Columbus, OH, USA, Oct. 6–11, 2013.

[9] B. Gibson-Dunne, G. Brzezina, J. Smithson, K. Oueng, and A. Momciu, "Methodology and practical considerations for the implementation of the three-antenna method in a spherical near-field range," in *Proc. Antenna Meas. Techn. Assoc. Symp. (AMTA)*, Denver, CO, USA, Oct. 9–14, 2022, pp. 1–6.

[10] J. E. Hansen, Ed., *Spherical Near-Field Antenna Measurements*. London, U.K.: Peter Peregrinus, 1988.

[11] D. Sánchez-Escuderos, M. Baquero-Escudero, J. I. Herranz-Herruzo, and F. Vico-Bondía, "Iterative algorithm for probe calibration in spherical near-field antenna measurement," *IEEE Trans. Antennas Propag.*, vol. 58, no. 9, pp. 3069–3074, Sep. 2010.

[12] T. Laitinen, S. Pivnenko, J. M. Nielsen, and O. Breinbjerg, "Theory and practice of the FFT/matrix inversion technique for probe-corrected spherical near-field antenna measurements with higher-order probes," *IEEE Trans. Antennas Propag.*, vol. 58, no. 8, pp. 2623–2631, Aug. 2010.

[13] T. B. Hansen, "Spherical near-field scanning with higher-order probes," *IEEE Trans. Antennas Propag.*, vol. 59, no. 11, pp. 4049–4059, Nov. 2011.

[14] S. Pivnenko, J. M. Nielsen, O. Breinbjerg, T. Laitinen, and T.B. Hansen, "Comparison of the FFT/matrix inversion and system matrix techniques for higher-order probe correction in spherical near-field antenna measurements," in *Proceedings of the 33rd ESA Antenna Workshop on Challenges for Space Antenna Systems*, Noordwijk, The Netherlands, Oct. 18–21, 2011.

[15] A. Hadjidimos, "Successive overrelaxation (SOR) and related methods," *Journal of Computational and Applied Mathematics*, vol. 123, no. 1, pp. 177–199, Nov. 2000.

[16] D. M. Young, *Iterative Solution of Large Linear Systems*. New York: Academic Press, 1971.

[17] *Altair Feko.* (2021). Altair Engineering, Inc. [Online]. Available: https://www.altair.com/feko

[18] M. A. Saporetti, L. J. Foged, M. Sierra-Castañer, S. Pivnenko, R. Cornelius, and D. Heberling, "Description and results: Antenna measurement facility comparisons," *IEEE Antennas Propag. Mag.*, vol. 59, no. 3, pp. 108–116, Jun. 2017.

[19] G. Mayhew-Ridgers, P. A. van Jaarsveld, and J. W. Odendaal, "Extended near-field capabilities for the compact antenna test range at the University of Pretoria," in *Proceedings of the International Conference on Electromagnetics in Advanced Applications (ICEAA)*, Cape Town, South Africa, Sep. 5–9, 2022.

[20] A. C. Ludwig, "The definition of cross polarization," *IEEE Trans. Antennas Propag.*, vol. AP-21, no. 1, pp. 116–119, Jul. 1973.

[21] O. Breinbjerg, K. Kaslis, and J. M. Nielsen, "An experimental and computational investigation of high-accuracy calibration techniques for gain reference antennas," in *Proc. Antenna Meas. Techn. Assoc. Symp. (AMTA)*, Atlanta, GA, USA, Oct. 15–20, 2017.

[22] G. Mayhew-Ridgers, J. W. Odendaal, and J. Joubert, "Improved diffraction model and numerical validation for horn antenna gain calculations," *International Journal of RF and Microwave Computer-Aided Engineering,* vol. 19, no. 6, pp. 701–711, Nov. 2009.

Gordon Mayhew-Ridgers (Senior Member, IEEE) received the B.Eng., B.Eng.(Hons), M.Eng., and Ph.D. degrees in electronic engineering from the University of Pretoria, Pretoria, South Africa, in 1994, 1996, 1998, and 2004, respectively.

From 1995 to 1997, he was an Engineer with Telkom in South Africa. Since 1998, he has been with Vodacom in South Africa, where he is currently a Principal Engineer. He is primarily involved with all aspects of antenna characterization, together with the modeling and measurement of RF phenomena in wireless networks. His interests include computational electromagnetics as well as the development and application of near-field antenna measurement systems.

Paul A. van Jaarsveld (Member, IEEE) received the B.Eng. and M.Eng. degrees in electronic engineering from the University of Pretoria, Pretoria, South Africa, in 1993 and 1996, respectively.

From 1996 to 2000, he was a Microwave Design Engineer with SAAB-Grintek Avitronics in South Africa. Since 2001, he has been with Vodacom in South Africa, where he is currently a Principal Engineer with a focus on antenna metrology. His field of interest includes MIMO, software defined radios, and the development of near-field measurements systems to characterize active antennas with modulated signals.

Johann W. Odendaal (Senior Member, IEEE) received the B.Eng., M.Eng., and Ph.D. degrees in electronic engineering from the University of Pretoria, Pretoria, South Africa, in 1989, 1991, and 1994, respectively.

From September 1993 to April 1994, he was a Visiting Scientist with the ElectroScience Laboratory at the Ohio State University. From August to December 2002, he was a Visiting Scientist with CSIRO Telecommunications and Industrial Physics in Australia. Since May 1994, he has been with the University of Pretoria, where he is currently a Full Professor. His research interests include electromagnetic scattering and radiation, compact-range measurements, and signal processing. He is also Director of the Centre for Electromagnetism at the University of Pretoria.

Prof. Odendaal is a member of the Antenna Measurement Techniques Association (AMTA) and registered as a Professional Engineer in South Africa.